

INSTABILITIES AND CLUMPING IN SN 1987A. I. EARLY EVOLUTION IN TWO DIMENSIONS

BRUCE FRYXELL

Steward Observatory and Departments of Physics and Astronomy, University of Arizona

EWALD MÜLLER

Max-Planck-Institut für Astrophysik

AND

DAVID ARNETT

Steward Observatory and Departments of Physics and Astronomy, University of Arizona

Received 1990 March 9; accepted 1990 June 27

ABSTRACT

Two-dimensional hydrodynamic calculations of SN 1987A (Arnett, Fryxell, and Müller 1989) have been confirmed and extended. A systematic sequence of calculations, differing only in resolution, is presented in order to permit differentiation between physical and numerical effects. This sequence also makes possible comparison with other work done with different numerical techniques. Shortly after the shock reaches the surface of the presupernova, the spherical symmetry of the mantle is severely fractured as a result of Rayleigh-Taylor instabilities. No special asymmetry in the explosion is required. This fracturing appears long before significant decay of ^{56}Ni occurs. The presence of the instability seems to be rather insensitive to the initial presupernova structure (provided it is reasonably accurate). The amount of mixing of various elements is determined by including 10 separate fluids in the calculations enabling us to determine the distribution of each element in velocity space. The amount of mixing and clumping is somewhat sensitive to the choice of seed perturbation. However, it appears that perturbations of physically reasonable amplitude will provide sufficient mixing and clumping to explain the earlier than expected observations of X-rays and γ -rays and the shape of the light curve. The velocities of heavy elements are lower than observed for an explosion energy of 1.0×10^{51} ergs, but are interestingly close for 2.0×10^{51} ergs, and will increase after ^{56}Ni decay heats the inner regions. The degree of clumping obtained would also affect estimates of mass from modeling the light curves of SN Ib.

Subject headings: hydrodynamics — shock waves — stars: evolution — stars: individual (SN 1987A) — stars: interiors — stars: supernovae

I. INTRODUCTION

The idea that Type II supernovae would develop instability toward nonradial motion and asymmetric structure during the explosion is not new (e.g., Falk and Arnett 1973; Chevalier 1976; Bandiera 1984). Although Galactic supernova remnants provided interesting hints, direct and convincing observational evidence of such behavior only became available with the advent of Supernova 1987A in the Large Magellanic Cloud. The earlier than expected detection of X-rays (Dotani *et al.* 1987; Sunyaev *et al.* 1987; Wilson *et al.* 1988) and γ -rays (Matz *et al.* 1988) can most easily be explained if radioactive ^{56}Co had been mixed from the interior regions of the star into the envelope where the optical depth was much smaller, or that clumping had opened up paths of much smaller optical depth. Moreover, the width of the infrared spectral lines of Fe II (Erickson *et al.* 1988; Spyromilio *et al.* 1990; Haas *et al.* 1990), Ni II, Ar II, and Co II (Rank *et al.* 1988; Witteborn *et al.* 1989) indicate that these elements were mixed from the slower moving inner regions of the supernova into the faster moving outer layers; the velocity of these heavy elements is about equal to that of the supernova photosphere in 1987 April, when there was no evidence for Fe and Co overabundances in the optical spectra (Höflich 1988*a, b*). The indication from hydrogen-line spectra at day 221 of expansion velocities as low as 800 km s^{-1} suggests that this material was bypassed by faster moving matter from the inner regions (Höflich 1988*b*). Further, optical data on lines of hydrogen (Blanco *et al.* 1987; Larson *et al.* 1987; Phillips 1988; Phillips and Heathcote 1989),

sodium (Hanuschik, Thimm, and Dachs 1988), and oxygen (Stathakis and Cannon 1988) suggest asymmetric motion in the ejecta. The shape of the light curve is also indirect but strong evidence of the need for mixing to occur (Arnett 1988*a, b*; Woosley 1988; Shigeyama and Nomoto 1990).

With the increasing accessibility of supercomputers, and especially with the development of more powerful numerical algorithms, it is now possible to do realistic calculations of such behavior in two and, to a limited extent, three dimensions (Arnett, Fryxell, and Müller 1989, hereafter AFM; Arnett, Fryxell, and Müller 1990; Müller, Fryxell, and Arnett 1990*a*, hereafter MFA; Hachisu *et al.* 1990). Critical reviews of the commonly used methods have appeared (Woodward and Colella 1984; Hawley, Smarr, and Wilson 1984; Fryxell, Müller, and Arnett 1989). The results may be summarized as follows: the piecewise parabolic method (PPM) of Colella and Woodward (1984) has 7 to 12 times better linear resolution than older methods (such as Lax-Wendroff) for typical stellar physics problems and about a factor of 2 better resolution than the best new methods with which we are familiar. To reproduce the results described below, which primarily used a 500^2 grid, with the older methods would require grid sizes between 3500^2 and 6000^2 . These are perhaps beyond the capability of computers currently available. Even the newer methods would require a grid of 1000^2 . Such calculations could be done on current computers, but they would be needlessly expensive.

In what follows, we will present a detailed discussion of new calculations of instabilities, mixing, and clumping in the ejecta

of SN 1987A beyond those commented on briefly in AFM. Here we restrict our discussion to two-dimensional results using a cylindrical grid; results for a spherical grid (in two and three dimensions) will be presented separately (Müller, Fryxell, and Arnett 1990b). This paper is focused upon the primary numerical results for density and compositional structures; for reasons of space, more advanced analysis of the velocity structure is deferred to a later paper.

II. COMPUTATIONAL METHOD

The calculations were done using the PROMETHEUS computer code, which is described in Fryxell, Müller, and Arnett (1989). This code solves the equations of hydrodynamics on an Eulerian grid (either fixed or moving) by the piecewise parabolic method (PPM) of Colella and Woodward (1984). A detailed comparison of PPM with other schemes has been given by Woodward and Colella (1984) for both one-dimensional and two-dimensional flow with strong shocks; they discuss artificial viscosity methods, linear hybridization (e.g., Boris and Book 1973), and Godunov methods (Godunov 1959) as well. Additional comparisons for one-dimensional test problems of both reactive and nonreactive flows can be found in Fryxell, Müller, and Arnett (1989). PPM showed significantly better results than any of the other methods tested for a given level of computer resources.

PROMETHEUS represents an extension of the original PPM method in three important ways: (1) it includes an arbitrary number of separate fluids which are used to keep track of the amount of mixing of various nuclear species (10 different species were included in the calculations described here), (2) a nuclear reaction network has been included (which is not relevant on the time scales considered here), and (3) modifications were made to treat a realistic (non-gamma law) equation of state (Colella and Glaz 1985).

The code uses sophisticated techniques to obtain high-resolution and resolve fine structure. Artificial viscosity is not required to stabilize shocks, and as a result, shocks are spread over only one or two zones. This is accomplished by solving Riemann's problem at zone interfaces in order to obtain accurate jump conditions across the shocks. Resolving contact discontinuities is a special problem for Eulerian methods. Shocks have a self-steepening mechanism which keeps them from spreading more than several zones, even with very diffusive methods. However, contact discontinuities continue to spread diffusively without limit in most Eulerian codes. PPM solves this problem by including a special algorithm which detects regions in the flow containing composition (and density) discontinuities and keeps them as sharp as possible. This is particularly important in the calculations presented here, since excessive numerical mixing of the different fluids in the calculations must be avoided. However, this procedure is even more important for obtaining an accurate representation of the density gradients which drive the instability. Without the discontinuity-sharpening mechanism, it would take a much larger grid to resolve the dynamics of the instability.

Figure 1 shows a comparison of the amount of diffusive spreading of such discontinuities for PPM and several other widely used hydrodynamics methods. The curves labeled "Lax-Wendroff" and "Donor cell" are representative of the widely used Eulerian methods of a few years ago. "SADIE" is a second-order alternating direction explicit hydrodynamics code developed by Arnold (1985) for multidimensional problems; it uses the flux-vector splitting method of van Leer (1982)

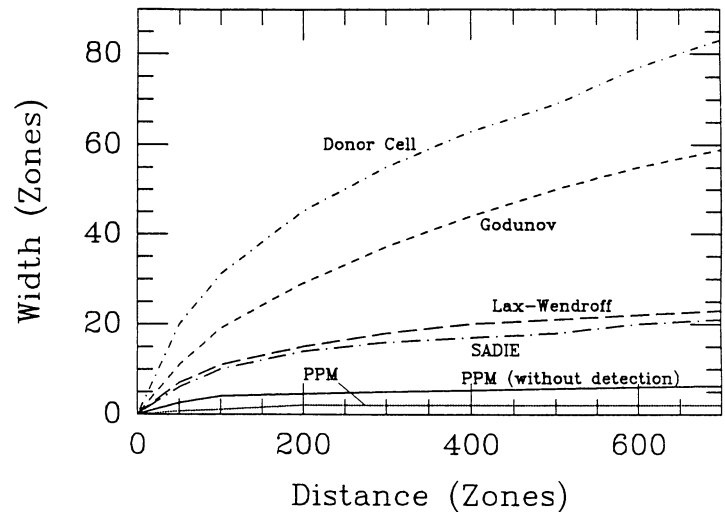


FIG. 1.—The rate at which Eulerian schemes spread contact discontinuities. The discontinuity is a simple step in composition, in pressure equilibrium, which propagates through the grid. Nothing should happen but the translation of this step in space. After the discontinuity has propagated through 700 zones, it has been spread over only two zones by PPM, while, at the other extreme, donor cell has produced a discontinuity that is more than 80 zones wide.

to calculate the fluxes in the advection terms, and the method of Beam and Warming (1978) to advance the equations in time to second-order accuracy. The Lax-Wendroff method (Lax and Wendroff 1960, 1964) has been widely used in astrophysics. The curves show the width (in zones) of the discontinuity versus the number of zones through which the discontinuity has moved. With the first-order methods (donor cell and Godunov), the discontinuity continues to spread rapidly as it propagates, with the error increasing with the number of zones traversed. For Lax-Wendroff and SADIE the curve flattens out somewhat, so the discontinuity is about 14 zones wide after 200 zones traversed, and 24 zones wide after 700. PPM (without discontinuity detection) does considerably better, with the discontinuity spreading over only five zones after it has propagated 200 zones. The discontinuity then spreads only two additional zones after propagating an additional 500 zones. The results for PPM with discontinuity steepening (*bottom curve*) show that the discontinuity spreads quickly over two zones, but no additional spreading takes place, even after 700 zones have been traversed. For problems such as this, PPM has a factor of 7 to 12 times better linear resolution than Lax-Wendroff and SADIE and a factor of more than 40 better than Donor Cell. These results are consistent with those of Woodward and Colella (1984).

This has important implications both for accuracy and for efficiency of calculation: (1) for more diffusive methods, the numerical diffusion will probably dominate the real physical mixing; and (2) the computer resources needed for accurate calculations become extraordinary. The amount of computer time needed to calculate a two-dimensional flow is proportional to the *cube* of the number of zones needed in each dimension; for a three-dimensional flow, the computer time required scales as the *fourth* power of the number of zones needed in each dimension (the extra power of the number of zones is due to stability limitations on the time step size). Because these calculations (especially in three dimensions) are near the limit attainable with current supercomputers, it is clear that using a

method which is inferior in resolution can have disastrous consequences. To be explicit, consider a Lax-Wendroff method: to reproduce the 500^2 results quoted below would require about $7^2 = 49$ times more zones (3500^2), and assuming a factor of 4 greater speed per point for the simpler method, $7^{3/4} \approx 86$ times more computer time.

The above comparisons do not include smooth-particle hydrodynamics methods (SPH), which have been used to address the same problems discussed in this paper. SPH applied to shock tube problems seem to be comparable in resolution to Lax-Wendroff (e.g., Monaghan 1985). However, comparison for multidimensional calculations is more difficult. It is clear that none of the SPH calculations have approached the resolution of the calculations described below. This is partially due to the fact that all the SPH calculations were performed using three spatial dimensions, making it difficult for them to compete with the linear resolution obtainable in a two-dimensional calculation without using enormous amounts of computer resources. Nevertheless, it would be interesting to determine, for example, how many particles are necessary for SPH to resolve the Rayleigh-Taylor "mushroom caps" (see below).

Although the complexity of PPM adds to both the initial effort in software development and the ongoing effort in adding new physics, the effort is clearly worthwhile, especially for two- and three-dimensional problems. See Colella and Woodward (1984), Woodward and Colella (1984), and Fryxell, Müller, and Arnett (1989) for more details. The code is more than 95% vectorized on the Cray-2 computer and runs at a speed of about 100 Mflops on one cpu. On a number of parallel machines (Cray, Convex, IBM), the code has obtained more than 90% of the theoretical speedup.

III. INITIAL MODEL

a) *The Basic Dilemma*

We do not have a reliable theory for the explosion mechanism of SN 1987A. Despite many pioneering efforts, there is no reproducible, generally agreed upon numerical simulation of the event. The neutrino data suffers from such severe statistical errors, due to the small number of counts, that it provides little enlightenment for such subtle questions. This leaves more freedom than desirable for initiating numerical simulations; it may be that we must use observations of the asymmetries and simulations of the event to infer details of the explosion mechanism itself.

It is easy to make the ejecta nonspherical by making the instigating explosion nonspherical. This is simply an assumption, and provides little insight into the cause of the asymmetry itself. Chevalier and Soker (1989) have examined the implications of a nonspherical explosion on envelope expansion, and related their results to observations of polarization; they felt that their models did not indicate a cause for the asymmetry. Yamada and Sato (1990) have calculated the hydrodynamics of a nonspherical shock wave as well, but, as they used only a first-order scheme and 12 angular zones, their resolution is too poor to give clear results.

b) *The Presupernova*

Observations of the progenitor star, Sanduleak $-69^\circ 202$, show that the presupernova had a luminosity of $L \approx 10^5 L_\odot$ and a spectral classification of B3 I, corresponding to an effective temperature of about 16,000 K. The luminosity implies a

He core mass of $6 M_\odot$, and taken with the effective temperature, a radius of $R \approx 3 \times 10^{12}$ cm. This is in excellent agreement with the values needed to explain the early light curve, temperatures, and velocities (e.g., Arnett 1988a, b). The explosion energy required is $1-2 \times 10^{51}$ ergs for $15 M_\odot$ ejected (Arnett 1987). The total mass must be less than about $20 M_\odot$. For abundances in the range of 0.1 of solar to solar, a $20 M_\odot$ star will develop a luminosity close to $L \approx 10^5 L_\odot$ at the end of its lifetime (after $^{12}\text{C} + ^{12}\text{C}$ burning, the luminosity does not change significantly), with (1) negligible mass loss and (2) semi-convection occurring on a finite time scale (Arnett 1991, in preparation). Inclusion of the latter effects, and overshooting, allows less massive stars to attain such luminosities. However, estimates of the hydrogen mass as well as simulations of the explosion constrain the amount of mass loss to be fairly small; a hydrogen envelope mass of order $10 M_\odot$ or more is suggested (see Arnett *et al.* 1989, hereafter ABKW, for details), and $14 M_\odot$ is consistent (essentially no mass loss). A few M_\odot lost prior to explosion is a reasonable guess; observations suggest that the star lost mass as a red supergiant before it exploded (Kirshner 1988). The neutrino signal (Hirata *et al.* 1987; Bionta *et al.* 1987) was consistent with the formation of a neutron star of about $1.5 M_\odot$ or so (Arnett 1987). Thus, subtracting this from the He core mass, about $4.5 M_\odot$ of matter inside the hydrogen shell was ejected. Thus, from the observations the total mass ejected is inferred to be $14-20 M_\odot$. The initial model chosen here was one which would give an acceptable reproduction of the light curve (Arnett 1988a, b). We chose a post- $^{12}\text{C} + ^{12}\text{C}$ burning star of $15 M_\odot$ and "LMC" abundances (one-fourth solar); this had a radius of $R = 3 \times 10^{12}$ cm.

c) *Initiation of the Explosion and Construction of Two-Dimensional Models*

The stellar model was interpolated for $0 < r < 0.1 R$ onto an equidistant Eulerian grid with $\Delta r = 5.0 \times 10^7$ cm. This corresponds to 6000 zones in the innermost 10% of the star (by radius), or 60,000 zones if the entire star had been zoned uniformly. The explosion energy, which was deposited into the inner few zones, was divided equally between kinetic and thermal components; that is, the energy was put in as a propagating shock. Hence the total mass ejected was $15 M_\odot$, with $4 M_\odot$ of matter from inside the hydrogen shell. For the calculations described below, an explosion energy of 1.0×10^{51} ergs was used (the total energy change was actually slightly higher, 1.13×10^{51} ergs, because gravity was neglected). In retrospect, an energy of 2.0×10^{51} ergs might have been a better choice. The propagation of the shock was then calculated up to a time $t = 300.3$ seconds using a one-dimensional version of the PROMETHEUS code. The shock at this time is still within the innermost 10% of the star. Note that entropy errors can result from incautious initiation of the explosion, and these will affect the subsequent stability. However, our results were not found to be particularly sensitive to the initial distribution of explosion energy. The density, pressure, and velocity profiles at $t = 300.3$ seconds are plotted in Figure 2 both as a function of radius (*top*) and as a function of mass (*bottom*). The extremely narrow density spike could only be resolved by using an extremely finely zoned grid. Even on relatively fine grids of 1000 zones, the peak density could be a factor of 2 lower, which would have a significant influence on the development of the instability.

Calculating the earliest stages of the explosion in one dimension has a number of advantages. The density spike could not

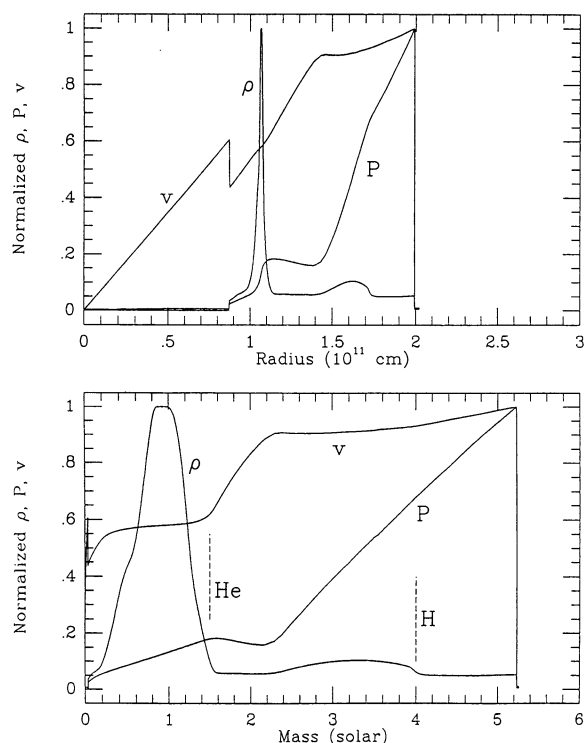


FIG. 2.—Snapshots of the normalized density (ρ), pressure (P) and velocity (v) for the $15 M_{\odot}$ explosion as a function of radius (top) and mass in solar units (bottom), taken 300 s after the beginning of the explosion ($E = 10^{51}$ ergs). At this stage, the dynamics need be calculated only for the innermost 10% (in radius) of the star ($R/10 = 3 \times 10^{11}$ cm and $M_r = 6 M_{\odot}$). The Eulerian grid consists of 6000 equidistant radial zones ($\Delta r = 5 \times 10^7$ cm). The matter is Rayleigh-Taylor unstable just inside the indicated interfaces (vertical dashed lines) for both “metal”/He and He/H. Notice the sharp density spike (top) and the central void which occupies the inner third of the stellar radius.

be resolved on a two-dimensional grid without using an unreasonably large number of zones. In addition, due to the very large temperature and correspondingly high sound speed in the central zones immediately after the explosion, the time step required for numerical stability is extremely small. Following this stage on the two-dimensional grids used for the later stages of the explosion would be quite expensive. Finally, it is impossible to accurately represent a spherical shock on a cylindrical grid when the shock radius is only a few zones. This would introduce large perturbations into the flow which would dominate the imposed seed perturbations (see below). The growth rate of the instability being studied here is sufficiently small during this initial period that the results are not significantly altered by this approach. In fact, the instability does not grow to a significant amplitude in our simulations until after $t = 2000$ s. Instabilities which occur either earlier or later than the times considered here will be the subject of future papers.

The next step was to obtain a one-dimensional model for the entire star at $t = 300.3$ s. This was accomplished by interpolating the model onto a one-dimensional grid of 500 zones, equidistant in radius, for the whole star. To do this, the inner 10% in radius came from the one-dimensional fine-zoned run, and the outer 90% came from the initial stellar model. Finally, the various two-dimensional models discussed below were obtained by mapping this one-dimensional grid of 500 zones onto a two-dimensional grid of appropriate zoning. Note that

this mapping drastically clipped the density spike for coarser grids, and contributed to the resolution effects discussed below.

IV. SEED: INITIAL PERTURBATIONS

a) The Dependence of Results upon Seed

Instabilities of the sort found here are the rapid growth of initial perturbations of a nonspherically symmetric nature. The structures which grow depend upon both the growth rate and upon these “seed” perturbations. Thus, the instability acts as an amplifier of preexisting asymmetries. An important reason for studying the instabilities is to discover whether it is possible to work back from observations of asymmetries in SN 1987A (and hopefully other supernovae) to probe the explosion itself.

In this paper, we deal with two sorts of seed perturbations (“seed” for short). One we add intentionally—we introduce a random perturbation of a specified amplitude in the radial velocity behind the shock in the 2D initial model. The wavelength scale for this perturbation is that of the grid itself. Other choices will be discussed separately (Müller, Fryxell, and Arnett 1990b). The other asymmetric perturbation is introduced by the grid; we use a cylindrical grid to represent an initially spherical explosion. The finite resolution of the grid introduces perturbations. Here both the amplitude and wavelength of these perturbations are determined by the grid. For relatively low-resolution calculations, this sort of perturbation is large, but it is usually damped out by numerical dissipation. On these grids, instabilities will not appear unless a large-amplitude seed perturbation is imposed. For higher resolution calculations, the grid perturbation is much smaller, but in this case, even if no additional seed is applied, numerical dissipation is small enough so that the instability will grow. However, instabilities resulting from seed perturbations with physically reasonable amplitudes will still dominate.

b) Estimates of Seed from $^{16}\text{O} + ^{16}\text{O}$ Shell

There are many possible sources of seed perturbations (see Arnett, Fryxell, and Müller 1989). To motivate the choice of a range of amplitudes for random seed, we may consider a likely case: asymmetry in the $^{16}\text{O} + ^{16}\text{O}$ shell when the shock hits it. We know of only one calculation which uses consistent zoning and microphysics from precollapse evolution through to the arrival of the shock at the $^{16}\text{O} + ^{16}\text{O}$ shell (Arnett 1986); we will use these results in what follows. In that sequence, the shell became very active as the core fell from under it and flashed before the shock arrived.

For example, at a mass coordinate $M_r = 3.07 \times 10^{33}$ g, the postshock temperature is $T_9 = 4.0$ and the density $\rho = 1.03 \times 10^7$ g cm $^{-3}$. The density scale height is $h = (d \ln \rho / dr)^{-1} = 2.0 \times 10^7$ cm and the radial coordinate is $r = 1.45 \times 10^8$ cm. The fluid velocity behind the shock is $u = 3.0 \times 10^9$ cm s $^{-1}$.

Let us make some crude estimates of the amplitude and wavelength of seed perturbations to get an idea of the magnitudes involved. First, we will make what seems to be an overly optimistic estimate, and then a minimal one, to infer the range of amplitudes of interest. The $^{16}\text{O} + ^{16}\text{O}$ shell flashes when the shock hits it. If it can maintain coherency only over a length of the order of the density scale height, for example, we would expect a wavelength $\lambda \simeq h$, or $\lambda/r \simeq \frac{1}{7}$ which is about 7 per radian or 10 per quadrant.

The amplitude of the perturbation might be estimated by comparing the energy released by the flashing of $^{16}\text{O} + ^{16}\text{O}$ to

that behind the shock, on the optimistic assumption that most of the thermonuclear energy goes into asymmetric motion. For an oxygen mass fraction of $X(^{16}\text{O}) = 0.58$ and an energy release of $q = 5 \times 10^{17} \text{ ergs g}^{-1}$ burned, the former is $X(^{16}\text{O})q = 2.9 \times 10^{17} \text{ ergs g}^{-1}$. The corresponding energy density behind the shock is near $u^2 = 10^{19} \text{ ergs g}^{-1}$. If we take this ratio (0.03) to be a measure of the energy of the perturbation, its amplitude would be $\sqrt{0.03} = 0.17$. The process would probably not be quite so efficient, so that we might regard this as a relatively high value.

Alternately, we might consider the preexisting asymmetries implied by the presence of convection in the $^{16}\text{O} + ^{16}\text{O}$ shell. The wavelength might be of the order of the mixing length, which, in turn, is of the order of the density scale height h again. The dimensionless amplitude might be expected to be of the order of the ratio of the convective speed ($v \simeq 1.0 \times 10^7 \text{ cm s}^{-1}$) to the local sound speed ($5 \times 10^8 \text{ cm s}^{-1}$), or 0.02. Note that the convective speed v is related to the convective flux by $F_{\text{conv}} \simeq \rho v^3$.

A satisfying estimate of the seed perturbations is difficult to make; a reliable model of the explosion mechanism would help. We take these estimates to be suggestive of the range of interest. Future calculations will allow us to more accurately determine the size of the seed perturbation which could be generated during the explosion.

V. THE DENSITY STRUCTURES

a) The Effect of Resolution upon Structure

In this section, we discuss the density structures which form as a result of the instability, and the way they are affected by numerical resolution and the initial seed perturbation. These results will help determine to what extent the structures are representative of correct physics and to what extent they are influenced by numerics. They also provide a basis for comparison with other calculations of these phenomena. Grid resolutions of 50^2 , 100^2 , 150^2 , 200^2 , 250^2 , 300^2 , 350^2 , 400^2 , and 500^2 were used. Random seed perturbations with amplitudes of 10%, 5%, 1%, and 0% were introduced in the radial velocity behind the shock. Because a random seed was used, the effective wavelength of the perturbation changed as a function of grid resolution, being 10 times larger for 50^2 than for 500^2 .

Figure 3 shows density contours at a time $t = 3.6$ hours for resolutions of 50^2 , 100^2 , 150^2 , and 200^2 in each of the four quadrants. The contours correspond to changes of 5% of the maximum density. For each calculation, axial symmetry about the vertical axis and equatorial symmetry along the horizontal axis were used. The 50^2 case (*lower right quadrant*) is not resolved. There is a feature along the vertical axis, but at this resolution it would be difficult to say if this is a Rayleigh-Taylor finger or a numerical problem associated with the symmetry axis. Actually, it is probably a combination of the two effects. There is also a slight hint of a finger developing along the horizontal axis. The 100^2 case (*lower left*) is slightly better, but hardly convincing. At 150^2 (*upper left*) there is a change in character, with four features clearly seen, although the grid size is still insufficient to resolve the structure of any of the features. With the 200^2 case (*upper right*), one of the features is finally resolved well enough to see the classic structure of a Rayleigh-Taylor finger, in which a "mushroom cap" forms at the end of the rising column as a result of the Kelvin-Helmholtz instability. This is common behavior for hot rising gas.

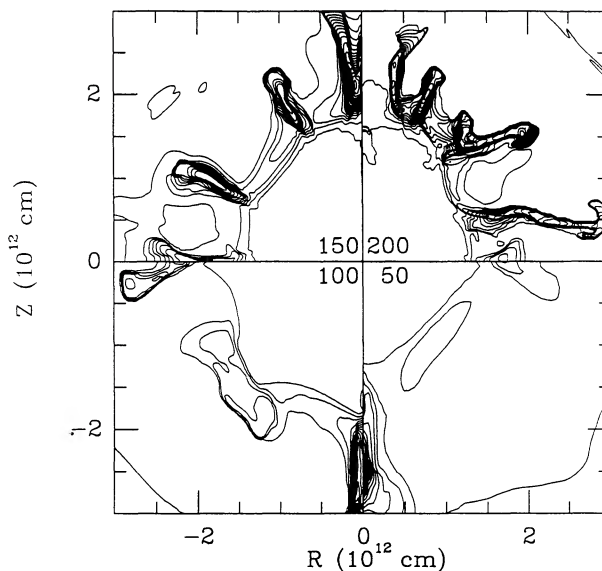


FIG. 3.—Density contours at a time $t = 3.6$ hr for resolutions of 50^2 , 100^2 , 150^2 , and 200^2 in each of the four quadrants. The contours correspond to changes of 5% of the maximum density.

The relatively sudden change in the character of the solution with increasing resolution is consistent with the notion that two factors are at work: (1) with poorer resolution, the numerical scheme is more dissipative, which tends to damp the instability; and (2) with higher resolution, the steep density and pressure gradients which drive the instability (e.g., Chevalier 1976) are better represented.

Figure 4 shows density contours at a time $t = 3.6$ hours for resolutions of 250^2 , 300^2 , 350^2 , and 400^2 . At 250^2 (*lower right*), all of the fingers are beginning to show "mushroom cap" structures. As the resolution is increased to 400^2 , there is an obvious improvement in the detail seen both in the fingers

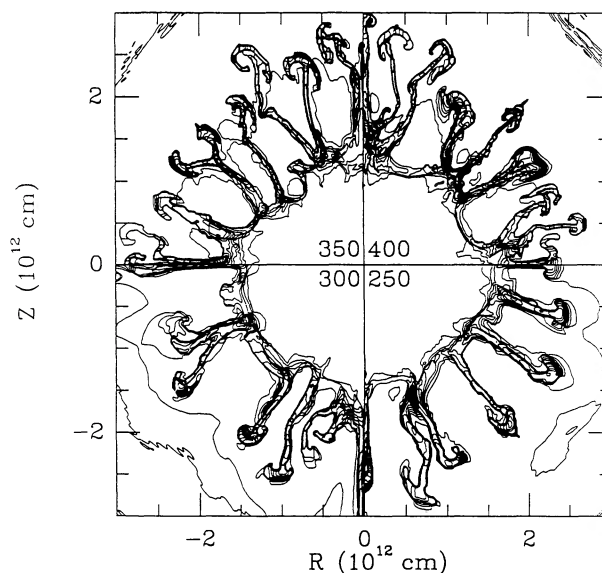


FIG. 4.—Density contours at a time $t = 3.6$ hr for resolutions of 250^2 , 300^2 , 350^2 , and 400^2 in each of the four quadrants. The contours correspond to changes of 5% of the maximum density.

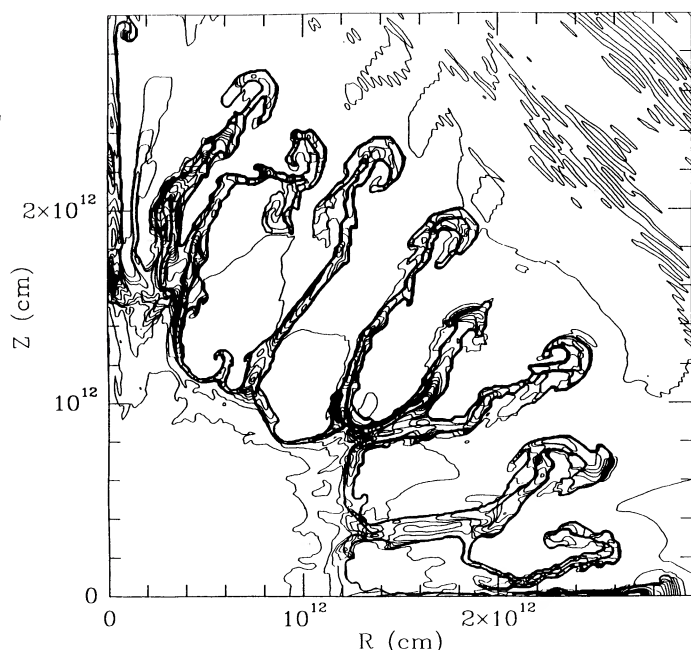


FIG. 5.—Density contours at a time $t = 3.6$ hr for the 500^2 case. The contours correspond to changes of 5% of the maximum density.

themselves and in the “mushroom caps.” It is interesting to note that, even though there is a substantial difference in the effective wavelength of the initial perturbation in these four calculations, the dominant wavelength of the instability does not change much, indicating that there is a preferred mode. However, the dominant wavelength of the instability can be changed by imposing a fixed wavelength on the initial perturbation. Likewise, if the explosion mechanism happens to perturb the flow with a wavelength different than that seen in these calculations, the results will be altered accordingly. This point is worthy of further investigation because it suggests that the observed asymmetries may contain information about the early asymmetries in the explosion and/or the presupernova structure.

The 500^2 case, shown in Figure 5, continues the trend. At low resolution (less than 300^2), the fingers tend to be primarily radial structures. At higher resolutions, there is an increasing tendency for the fingers to bend. This will make it possible for the fingers to interact with each other at later times, which will probably result in the formation of still more complex structures. In addition, small-scale ripples along the edges of the fingers, which are caused by Kelvin-Helmholtz instabilities, can be seen (especially at 500^2). If these instabilities continue to grow, they most likely will cause the fingers to break up into many individual clumps. It will be interesting to see if these trends continue for even higher resolution calculations.

b) The Effect of Seed Amplitude

To what extent are these features affected by the inherent grid error? The 500^2 case has sufficient resolution to represent a spherical shock with some accuracy. In Figure 6 the corresponding calculations for seeds of 0%, 1%, and 5% amplitude are shown. Calculating a spherical model on a cylindrical grid introduces a perturbation into the flow. The 0% case (Fig. 6a) illustrates the size of this perturbation. The shock (which has already propagated off the grid) remains perfectly spherical,

since this region of the flow is stable. However, the grid perturbation does cause oscillations to develop in the unstable region. Comparison with the 1% perturbation (Fig. 6b) shows that the effective amplitude of the grid perturbation on the 500^2 grid is much less than 1%. This is consistent with the idea that if the instability develops at a radius of about 200 zones, the effective amplitude of the grid perturbation should be on the order of $1/200 = 0.5\%$.

The 1% perturbation case shows much less nonlinear behavior than is seen when a 10% perturbation is used, as one might expect. The fingers are much broader and only one shows a hint of a mushroom cap. The number of fingers is about the same as in the 10% case (Fig. 5), so the primary effect of the smaller amplitude is that the features take longer to grow to the nonlinear regime. This slow growth is consistent with analytic considerations by Chevalier (1990). The nonlinearity is still increasing with time at this point in the calculation, and it is possible that the fingers will eventually evolve to look more like the 10% case. There is a competition between the expansion and the growth of the instability, and the time scales are comparable: it is not clear which wins. Also, since the fingers in the 1% case appear somewhat like the lower resolution calculations performed with a 10% seed, it is possible that nonlinear behavior might be observed at earlier times on higher resolution grids. The 5% calculation (Figure 6c) looks quite similar to the 10% case (Fig. 5) at this time. The length of the fingers has become very close to that obtained with a 10% seed. The main difference is that the fingers tend to be more nearly radial.

c) Comparison with Other Work

It is useful at this point to compare the results described above to other multidimensional hydrodynamic calculations which have appeared in the recent literature. The first attempts to study the problem involved looking for instabilities behind shocks propagating through polytropes. Nagasawa *et al.* (1989) performed three-dimensional calculations using a smooth-particle hydrodynamics code and found that significant clumping occurred behind the shock. Müller *et al.* (1989) calculated the same problem using a number of two- and three-dimensional finite-difference codes and found that the flow behind the shock was only very weakly unstable. Benz and Thielemann (1990) also studied the same problem with a three-dimensional smooth-particle hydrodynamics code and obtained results similar to those of Müller *et al.* (1989). They concluded that the instability found by Nagasawa *et al.* (1989) was most likely due to numerical effects connected with how the explosion is initiated. A more recent calculation by Nagasawa (1990) also showed that the strength of the instability depends on the method by which the explosion is initiated.

The first calculation using a realistic progenitor for SN 1987A was performed by Arnett, Fryxell, and Müller (1989). They found a violent Rayleigh-Taylor instability behind the shock which caused substantial mixing. Comparison of these results with the polytrope calculations of Müller *et al.* (1989), which were performed with the same numerical techniques, clearly shows that the results obtained for polytropes, while academically interesting, show little about instabilities which occur in supernovae.

Hachisu *et al.* (1990) also calculated the instabilities using a realistic presupernova model using a Lax-Wendroff method, which has much lower intrinsic resolution per grid point as discussed above. This was compensated for to some extent by

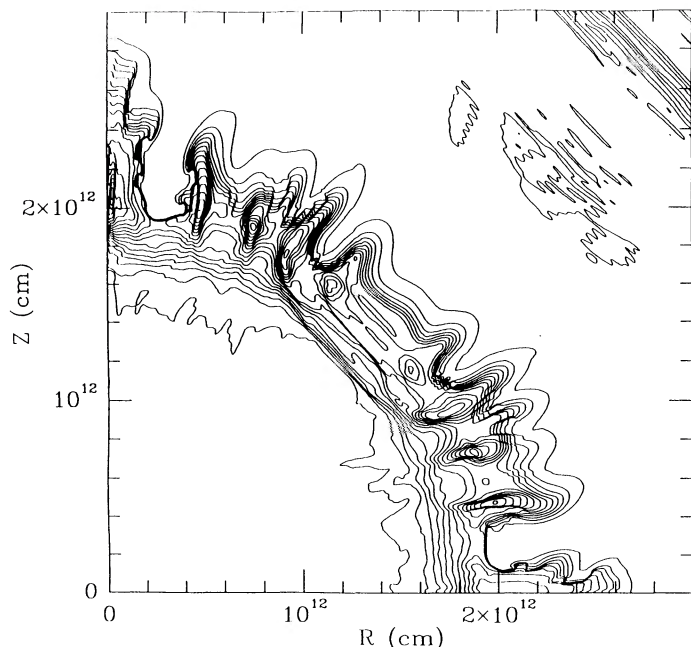


FIG. 6a

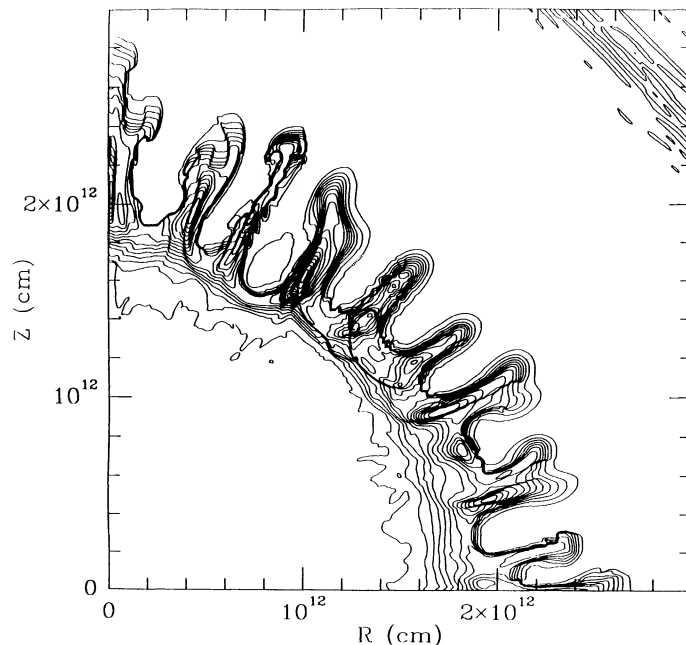


FIG. 6b

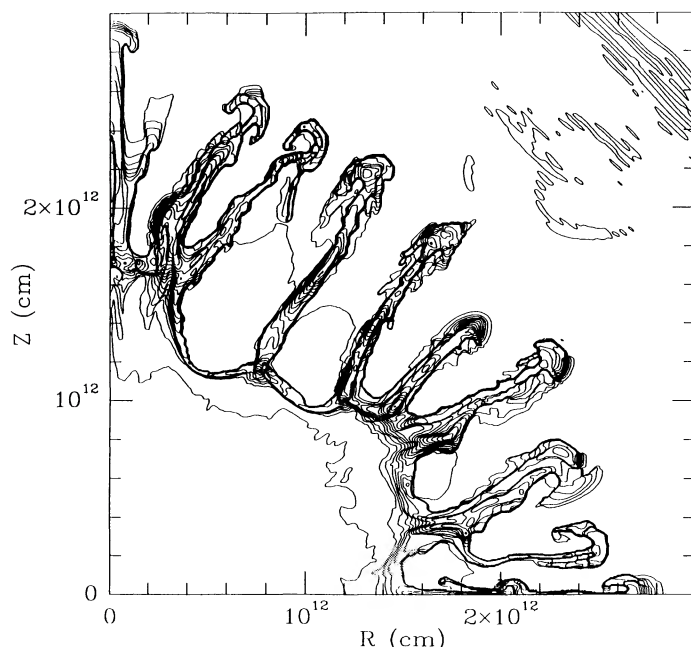


FIG. 6c

FIG. 6.—Density contours for the 500^2 case, corresponding to calculations using a seed perturbation of (a) 0%, (b) 1%, and (c) 5% amplitude, respectively.

use of a much larger number of zones and a faster computer (the Fujitsu VP-400 is quoted as 300 Megaflops per cpu, about 3 times the speed of PROMETHEUS on a Cray-2 cpu). In addition, several compromises were necessary. They calculated for a shorter time ($t = 3285$ s versus $13,000$ s), and used a smaller volume $R \approx 1 \times 10^{12}$ cm instead of $R \approx 3 \times 10^{12}$ cm. They did not follow the flow of fluids of different composition, but instead estimated the amount of mixing by a marker particle approximation. Finally, they used a gamma-law equation

of state instead of a mixture of radiation gas and ideal gas. While it is true that radiation pressure dominates most of the flow, the value of gamma for the gas within the Rayleigh-Taylor fingers is actually about 1.5.

Figure 7 is a comparable calculation done with PROMETHEUS (the time is slightly later, $t = 3.8 \times 10^3$ s; the number of zones in the active region is about 167^2). This is to be compared to Figure 2 of Hachisu *et al.* (1990), which has a zoning of 1025^2 in a quadrant; this is their random seed case. Although it used 1/6 the number of zones per dimension ($1/36$ in total), PROMETHEUS gave slightly better resolution. This is consistent with our estimate above of 7 to 12 for a Lax-Wendroff scheme—their features propagate through roughly 200 zones, which would imply a factor of 7 instead of 6. Although the two calculations used different initial stellar models and differed by a factor of 2 in seed amplitude, we do not expect these facts to alter the results significantly. We find that the results obtained with 5% and 10% seeds differ very little. The calculation shown in Figure 7 required approximately 15 minutes of Cray-2 time, while the calculation of Hachisu *et al.* (1990) required 2 hr on the VP-400, even with their simplified physics. The important feature of the Hachisu *et al.* (1990) work is that they had enough resolution to get beyond the “threshold” seen in Figure 3 above. To our knowledge, they are the only other group to have done so. They compensated for the poor resolution of their method by: (1) using many more zones, (2) concentrating them all in the inner third of the stellar radius, (3) calculating only the early stages of the evolution, and (4) using less accurate physics. The agreement with their results and Figure 7 is striking. There is every reason to believe that, if they contained their calculation a factor of 3 further in radius to the surface of the presupernova, their results would resemble our 500^2 case. Assuming a constant value of the time step, this would require 27 times more computer time (54 cpu hours on the VP-400 or 162 cpu hours on a Cray-2) and 9 times more memory.

In spite of the similarities between the results of Hachisu *et al.* (1990) and those presented here, there are some significant

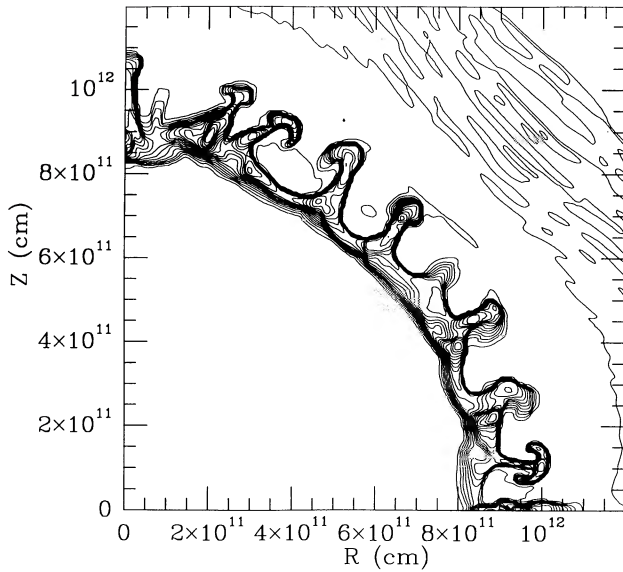


FIG. 7.—Density contours from a calculation done with PROMETHEUS using 167^2 zones in the active region (note the smaller radius than in other figs.), to be compared to Figure 2 of Hachisu and Nomoto (1990), which has a zoning of 1025^2 in a quadrant. The time for the PROMETHEUS calculation is later, $t = 3.8 \times 10^3$ s versus 3.285×10^3 s. PROMETHEUS obtained similar results with $1/6$ as many zones per dimension ($1/36$ total) because of inherently better resolution, especially of contact discontinuities.

differences. Most notable is the difference in the location of the instability. Hachisu *et al.* (1990) find an instability only at the hydrogen-helium interface. In our calculations, the instability also begins at the hydrogen-helium interface. However, a second instability, which has a larger growth rate, develops slightly later in time at the helium-metal interface. The fingers generated at the helium-metal interface eventually merge with those formed at the outer interface, giving the appearance of a single instability originating at the helium-metal interface. This is contrary to what was reported in Arnett, Fryxell, and Müller (1989). The same effect occurred in those calculations also, but was not originally noticed because of the lower resolution. The differences between the calculations in Hachisu *et al.* (1990), and those described here, other than those attributable to resolution, are most likely due to differences in the initial models and equations of state.

VI. MIXING

a) Macroscopic versus Microscopic Mixing

We should distinguish between microscopic mixing, which results in a composition which is homogeneous on the inter-particle scale, and macroscopic mixing which destroys the layered compositional structure of the presupernova, but in a clumpy, inhomogeneous way. Such a distinction may have important implications for interpreting observational data from SN 1987A and from supernova remnants.

To begin we consider some cross sections of interest (see also Fryxell, Müller, and Arnett 1989). For two particles of charge $Z_1 e$ and $Z_2 e$, we may define a Coulomb radius r_{coul} from $Z_1 Z_2 e^2 / 2r_{\text{coul}} = E$, where E is an appropriate energy. For example, for an atom, that energy would be the energy of the bound electron, so $E = p^2 / 2m_e$. Relating the momentum p to the radius, using the de Broglie wavelength, we have a cross

section of order

$$\sigma_{\text{atom}} = \pi a_0^2 Z_1 Z_2 = 0.88 \times 10^{-16} Z_1 Z_2 \text{ cm}^2,$$

where a_0 is the radius of the first Bohr orbit. However, at some temperatures of interest, atoms will be ionized. Taking $E = (3/2)kT$ gives

$$\sigma_{\text{coul}} = 1.01 \times 10^{-6} Z_1 Z_2 / T^2 \text{ cm}^2,$$

which is smaller for higher temperature.

At high temperatures and low density, radiative diffusion is characterized by Thomson opacity. Since $\sigma_{\text{thom}} = (8/3)\pi r_e^2 = 0.665 \times 10^{-24} \text{ cm}^2$, this cross section equals σ_{coul} at $T = [(3/2)Z_1 Z_2]^{1/2} \times 10^9 \text{ K}$. For lower temperature, heat diffuses faster than composition. At such temperatures and above, neutrino cooling dominates, so that, on evolutionary time scales, heat diffusion is unimportant by a large margin, as is compositional diffusion.

In a supernova, heat diffusion becomes important globally when the radiation diffusion time scale,

$$\tau_{\text{rad}} \simeq R^2 / 3\lambda c \simeq M\kappa / 4\pi R c,$$

equals the expansion time scale $\tau_{\text{exp}} = R/v$. For an average velocity $v \simeq 3 \times 10^8 \text{ cm s}^{-1}$, a radiative opacity $\kappa \simeq 0.2 \text{ cm}^2 \text{ g}^{-1}$, and a mass $M = 20 M_\odot$, this implies $R \simeq 3 \times 10^{15} \text{ cm}$, which corresponds to a time of $R/v \simeq 10^7 \text{ s}$. This is about the time of the second maximum for SN 1987A, which was due to the diffusive release of radiation from the heating caused by ^{56}Co decay. At such time the temperature inside the object is of order $T \simeq 10^5 \text{ K}$, so that σ_{coul} is larger than σ_{thom} by a factor of more than 10^8 . Compositional mixing by diffusion would only be important on small length scales, $r \simeq R \times 10^{-4}$ or less.

Further expansion results in cooling to recombination temperatures, so that σ_{atom} is the relevant cross section. The compositional diffusion time is:

$$\tau_{\text{comp}} \simeq M\kappa_{\text{comp}} / 4\pi R v_{\text{disp}},$$

where $\kappa_{\text{comp}} = N_{\text{atom}} \sigma_{\text{atom}} / \rho$. Observation (Hanuschik and Dachs 1987) and numerical experiment (AFM) give $v_{\text{disp}} \simeq 0.1v$. Equating τ_{comp} to the expansion time scale gives a radius $R \simeq 1.5 \times 10^{21} \text{ cm}$ and a time $R/v \simeq 1.5 \times 10^5 \text{ yr}$. By this time the ejecta have swept up significant surrounding matter, which adds another effect to the problem. We also note that microscopic mixing would drastically change the late time spectrum from what is observed (Fransson and Chevalier 1989).

It seems likely that the ejecta are mixed only macroscopically in young supernova remnants, and that evidence for their pre-explosion abundance patterns should survive in the inhomogeneous clumping. These patterns should provide information about the hydrodynamic phases we consider here.

b) The Composition Structures

What spatial and velocity structures in composition are predicted? Without the effect of the instability, the composition profile would consist of an inner region ($r < 10^{12} \text{ cm}$) where the heavy elements are concentrated. Surrounding this would be a spherical shell of almost pure ^4He . Outside this shell is the hydrogen-rich envelope. The effect of the instability is to break up the ^4He shell into knots of almost pure ^4He , while at the same time pushing the heavy elements outward along the Rayleigh-Taylor fingers into the hydrogen envelope, and bypassing some of the hydrogen-rich material in the regions between the fingers. Thus, the instability results both in the

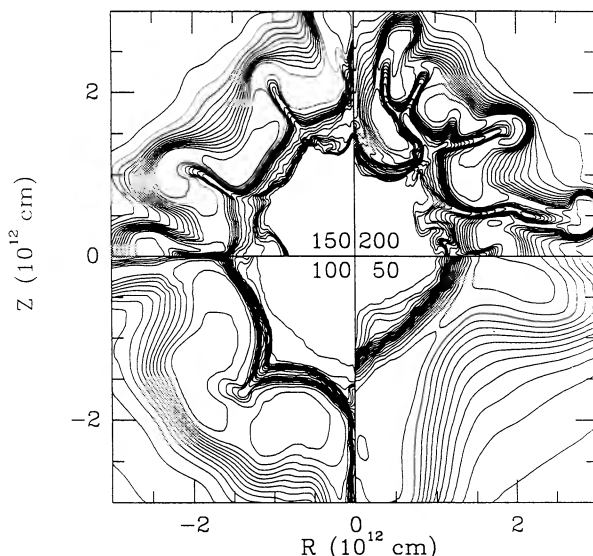


FIG. 8.—Mass fraction contours for ${}^4\text{He}$ at a time $t = 3.6$ hr for resolutions of 50^2 , 100^2 , 150^2 , and 200^2 in each of the four quadrants. A 10% random seed was used; this corresponds to Figure 3. The contours correspond to changes of 5% of the maximum abundance by mass. The inner region ($r < 10^{12}$ cm) is a “hole” devoid of ${}^4\text{He}$.

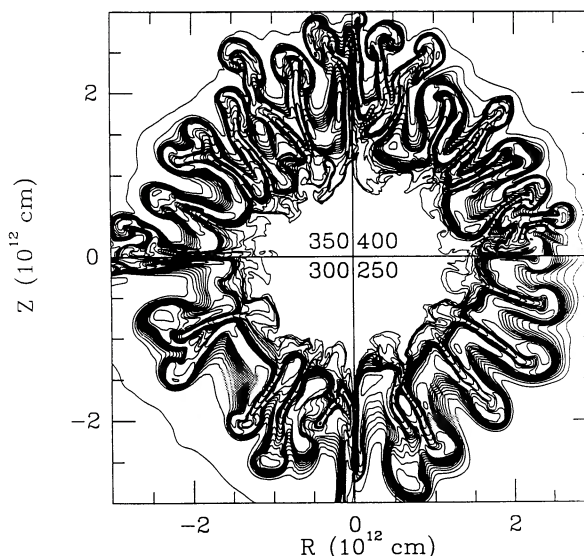


FIG. 9.—Mass fraction contours for ${}^4\text{He}$ at a time $t = 3.6$ hr for resolutions of 250^2 , 300^2 , 350^2 , and 400^2 . This corresponds to Figure 4.

formation of clumps of composition and in significant modification of the velocity distribution of the various elements.

Figure 8 shows contours of ${}^4\text{He}$ mass fraction at a time $t = 3.6$ hr for resolutions of 50^2 , 100^2 , 150^2 , and 200^2 in each of the four quadrants. A 10% random seed was used; this corresponds to Figure 3. The contours represent changes of 5% of the maximum abundance by mass. As before, the 50^2 case (lower right quadrant) is completely unresolved. The inner edge of the ${}^4\text{He}$ shell is too close to the origin, and the width of the shell has spread considerably. There is a hint of a couple of fingers of ${}^4\text{He}$ pushing outward, but it is hardly convincing. The 100^2 case (lower left) is slightly better. There is now a well-defined ${}^4\text{He}$ shell at the correct location and clear indication of a finger of heavy elements along the diagonal pushing into the ${}^4\text{He}$. At 150^2 (upper left) there are four well-defined fingers of heavy elements extending into the ${}^4\text{He}$ shell. This resolution also shows the first clear indication of some of the hydrogen-rich material being left behind by the faster moving fingers. With the 200^2 case (upper right), the flow has become so highly distorted that one can no longer consider the shape of the ${}^4\text{He}$ layer as a perturbation from the original spherical shell. The hydrogen-helium interface between the fingers (especially near the vertical axis) is now penetrating into the heavy element core.

Figure 9 shows abundance contours for ${}^4\text{He}$ at a time $t = 3.6$ hr for resolutions of 250^2 , 300^2 , 350^2 , and 400^2 . This corresponds to Figure 4. In addition to the steady increase in detail, there is a tendency for the hydrogen-helium interface to extend deeper into the star with increasing resolution. Also, although it is difficult to tell from the contour plots, there is an increasing tendency for the ${}^4\text{He}$ shell to fragment and form clumps of nearly pure ${}^4\text{He}$, concentrated primarily in the mushroom caps at the end of the fingers.

The 500^2 case (Fig. 10) continues the trend. At this time, only $t = 3.6$ hr after core collapse, the ${}^4\text{He}$ shell is deformed into a highly corrugated topology. This occurs with no significant

asymmetry in the explosion beyond that already implied by burning in the ${}^{16}\text{O} + {}^{16}\text{O}$ shell and convective motions. Radioactive decay of ${}^{56}\text{Ni}$ has not yet become an effective energy source, and any resulting instability will not appear until a few days after the explosion.

Figure 10 shows the corresponding results for a seed of 0%, 1%, and 10% amplitude on a 500^2 grid. The 5% case differs from the 10% case only in detail and is therefore not shown. The error of mapping onto a cylindrical grid, illustrated by the 0% case (Fig. 10a) introduces noticeable distortions in the shape of the ${}^4\text{He}$ shell. However, only a very small amount of penetration of the hydrogen and heavy elements into the ${}^4\text{He}$ shell has occurred. The differences for a 1% seed (Fig. 10b) are immediately apparent. The ${}^4\text{He}$ shell is now extremely rippled, and the fingers of heavy elements reach beyond the outer edge of the ${}^4\text{He}$ shell. Likewise, some hydrogen has penetrated to the outer edge of the heavy element core.

Figure 11 shows mass fraction contours for ${}^{16}\text{O}$ at a time $t = 3.6$ hr for resolutions of 50^2 , 100^2 , 150^2 , and 200^2 . A 10% random seed was used; this corresponds to Figures 3 and 8. The mass fraction of ${}^{16}\text{O}$ is high only in the inner regions, resembling a central “mesa.” As the resolution increases, the fingers of ${}^{16}\text{O}$ extend farther outward. With the 200^2 case, the fingers of ${}^{16}\text{O}$ (and other heavy elements) are punching completely through the ${}^4\text{He}$ shell into the hydrogen envelope.

Figure 12 shows mass fraction contours for ${}^{16}\text{O}$ at a time $t = 3.6$ hours for resolutions of 250^2 , 300^2 , 350^2 , and 400^2 . This corresponds to Figures 4 and 9. As the grid size is increased, the fingers of ${}^{16}\text{O}$ become increasingly pronounced and thin. The 500^2 case is shown in Figure 13 and continues the trend. Note that the concentration of ${}^{16}\text{O}$ decreases steadily from the central “mesa” to the ends of the fingers. The corresponding results for seeds of 0%, 1%, and 5% amplitude on a 500^2 grid are simply what might be expected after examining Figure 11. The results for ${}^{12}\text{C}$, ${}^{20}\text{Ne}$, ${}^{24}\text{Mg}$, and ${}^{28}\text{Si}$ are similar to those shown for ${}^{16}\text{O}$, although differing in details. To illustrate this, Figure 14 shows the 500^2 case for ${}^{24}\text{Mg}$. Notice the similarity to Figure 13.

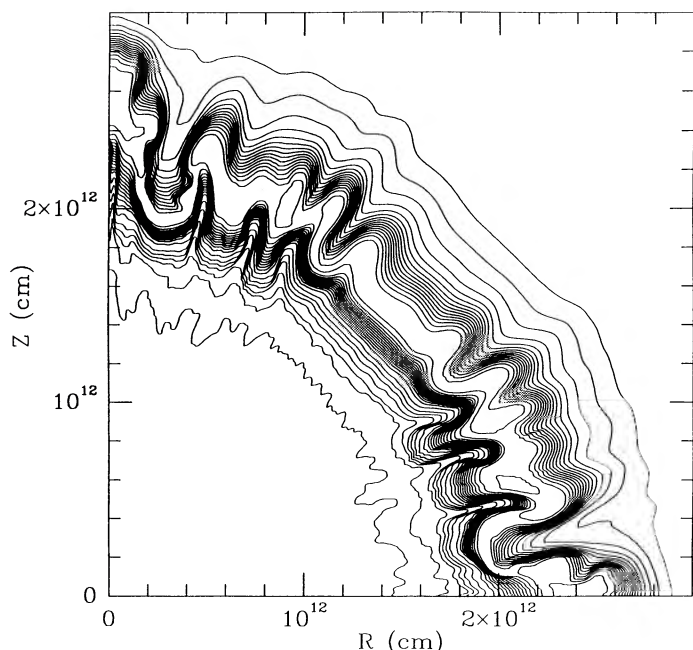


FIG. 10a

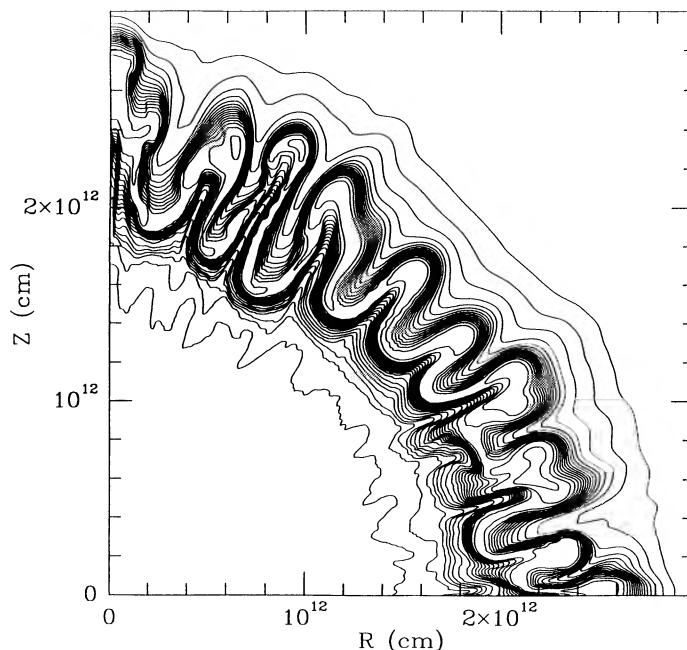


FIG. 10b

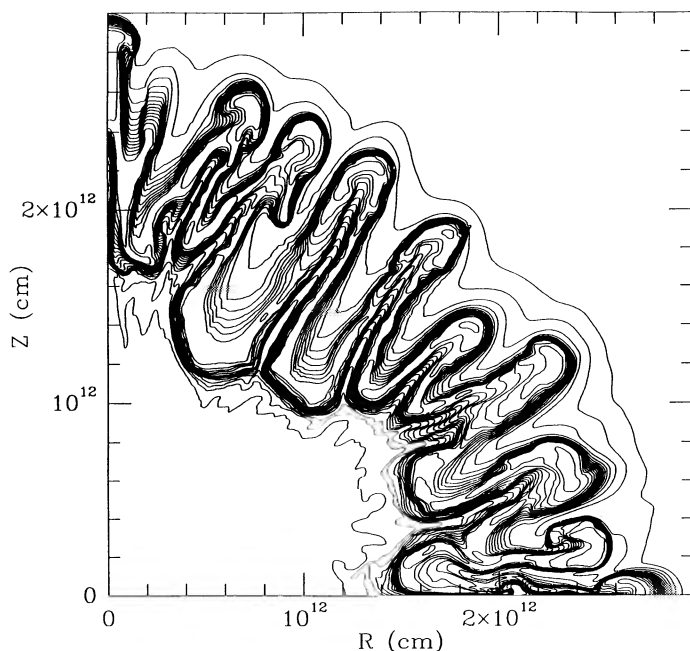


FIG. 10c

FIG. 10.—Mass fraction contours for ${}^4\text{He}$ at a time $t = 3.6$ hr for a seed of (a) 0%, (b) 1%, and (c) 10% amplitude on a 500^2 grid. The error of mapping onto a cylindrical grid (0% case) is small, lying below 1%, and does not give a pronounced effect. The 5% case is almost identical to the 10% case, and so is not shown.

VII. CLUMPING

a) Angular Variation in Attenuation

From the previous discussion of the density structure, it is clear that there is significant clumping of the matter. A useful

measure of this is the attenuation σ , which we define as

$$\sigma \equiv \int_0^R \rho \, dr.$$

This quantity is shown versus angle θ in Figure 15 for a resolution of 500^2 , an elapsed time of 1.3×10^4 s, and seed amplitudes of 0%, 1%, 5%, and 10%. Variations in σ from 2 to 5 occur. Even the 1% case shows peak to valley variations in σ of a factor of 2. These will have a profound effect upon models of the spectra: (1) Because of the clumping, γ -rays will escape more easily than would be expected from a density distribution which is uniform in angle: there are holes to escape through. (2) The X-ray spectra will be modified because the distribution of probabilities for multiple scatters will be modified (Fu and Arnett 1989; Kumagai *et al.* 1989; Bussard, Burrows, and The 1989). (3) The diffusion time for thermal photons will be shorter because the low-density lanes will allow faster escape: this is like a lower Rosseland mean opacity. Consequently, masses estimated from diffusion times (for example, from fitting light curves to spherically symmetric models) will be systematically too small. The amplitude of the error should be of the order of a factor of 2 for the inner regions by themselves, but will depend upon the detailed distribution.

b) Effects of Computational Resolution

In Figure 16 are shown snapshots of the attenuation σ versus angle θ for resolutions of 50^2 , 100^2 , 150^2 , and 200^2 , an elapsed time of 1.3×10^4 s, and a seed amplitude of 10%. The amplitude of the clumping reaches a roughly constant value for modest resolution (around 200^2), and changes little for better zoning. This may be seen in Figure 17, which is similar to Figure 16, but carries the resolution sequence through resolutions of 250^2 , 300^2 , 350^2 , and 400^2 . The wavelength of the variations in σ does continue to decrease somewhat for the better zoned cases.

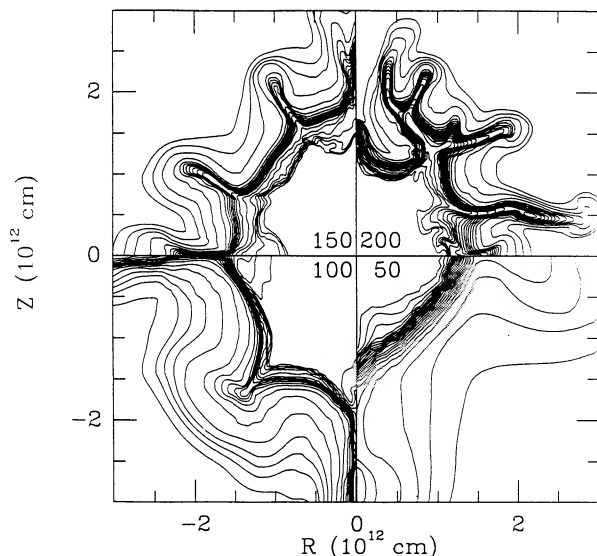


FIG. 11.—Mass fraction contours for ^{16}O at a time $t = 3.6$ for resolutions of 50^2 , 100^2 , 150^2 , and 200^2 in each of the four quadrants. A 10% random seed was used; this corresponds to Figures 3 and 8. The abundance of ^{16}O is high only in the inner regions, resembling a central “mesa.”

VIII. MIXING IN VELOCITY SPACE

a) Abundances in Velocity Space

The distribution in velocity space of the different elements is of direct observational interest in that it determines the shapes of absorption and emission lines. The present calculations are illustrative, but as yet provide a less than perfect basis for comparison with observations because of the following: (1) the decay of ^{56}Ni and ^{56}Co , which will add enough energy to modify the velocities significantly, has not yet occurred; (2) the fixed grid extending to $R = 3 \times 10^{12}$ cm allows faster moving matter to flow out of the computational volume (so that it is not graphed); and (3) the choice of explosion energy of

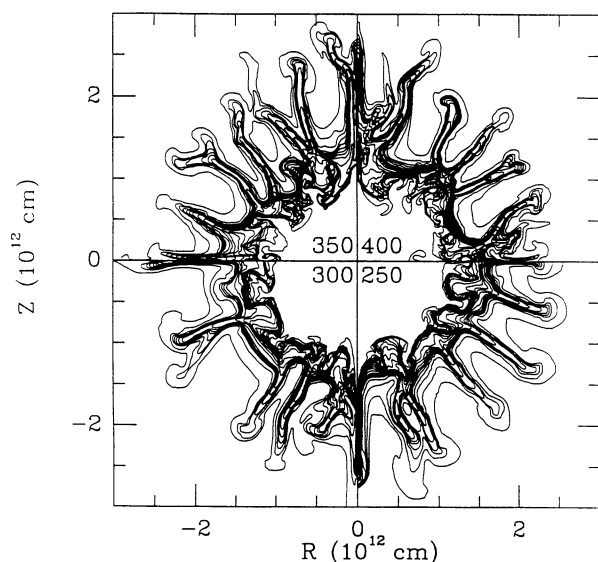


FIG. 12.—Mass fraction contours for ^{16}O at a time $t = 3.6$ hr for resolutions of 250^2 , 300^2 , 350^2 , and 400^2 . This corresponds to Figures 4 and 9. The fingers of ^{16}O become increasingly pronounced and thinner.

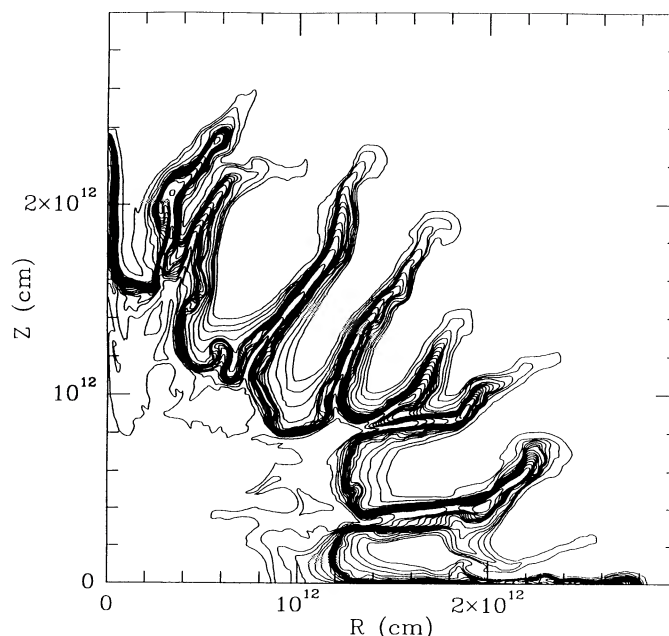


FIG. 13.—Mass fraction contours of ^{16}O at a time $t = 3.6$ hr for the 500^2 case.

1×10^{51} ergs is low, and could easily be 2×10^{51} ergs, which would scale the velocities upward by a factor of 1.4.

In Figure 18 are shown the abundances of four important nuclei (H , ^4He , ^{16}O , and ^{24}Mg , the latter being representative of ^{20}Ne and heavier nuclei). The results for ^{12}C resemble those for ^{16}O . The mass (in grams) per unit velocity interval dM/dv , is plotted versus radial velocity v . The different curves correspond to initial random seeds with amplitudes of 0% (grid noise), 1%, 5%, and 10%. The panels are labeled with the

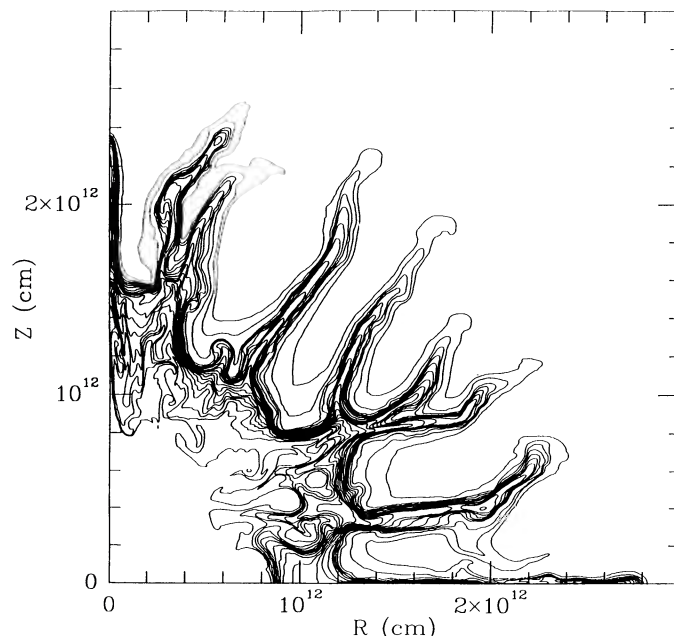


FIG. 14.—Mass fraction contours of ^{24}Mg at a time $t = 3.6$ hr for the 500^2 case. Notice the similarity to Figure 13.

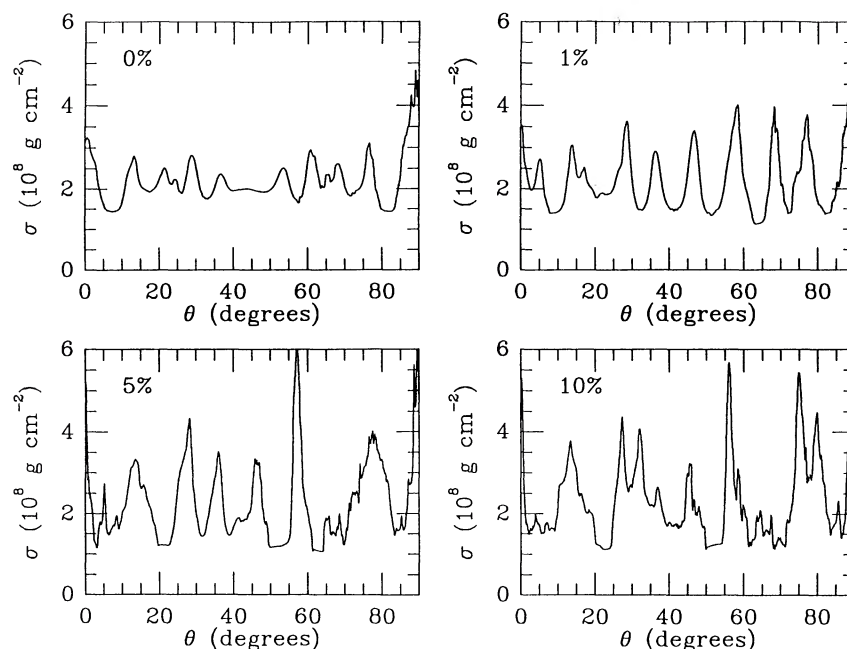


FIG. 15.—Attenuation σ (areal density) versus angle for a 500^2 zoning and seed amplitudes of 0%, 1%, 5%, and 10%

corresponding nucleus. In the case of hydrogen, the velocity is truncated at $v \simeq 2 \times 10^3 \text{ km s}^{-1}$ because faster moving hydrogen has left the computational grid at this time (13,000 s). The important effect here is the extension of the hydrogen velocities to low values, a result of the asymmetric motion. Even the 0% case (grid noise) shows some extension to low velocity ($v < 10^3 \text{ km s}^{-1}$), but it is more prominent for 5% and 10%. This smooths the global opacity in the region of what would have been the spherical shell of ^4He , and thereby smooths the light

curve, as suggested by comparison of the analytic solutions to observations (Arnett 1988*a, b*; Arnett and Fu 1989).

The ^4He distribution in velocity is spread to both higher and lower velocities. For this explosion energy, 1×10^{51} ergs, the peak of the dM/dv versus radial velocity curve moves from about 1000 to 1600 km s^{-1} , and significant amounts of ^4He move at $v < 800 \text{ km s}^{-1}$, as the value of the seed amplitude is changed from grid noise to 10%. For ^{16}O and ^{24}Mg , the behavior is similar; although they start at lower velocities,

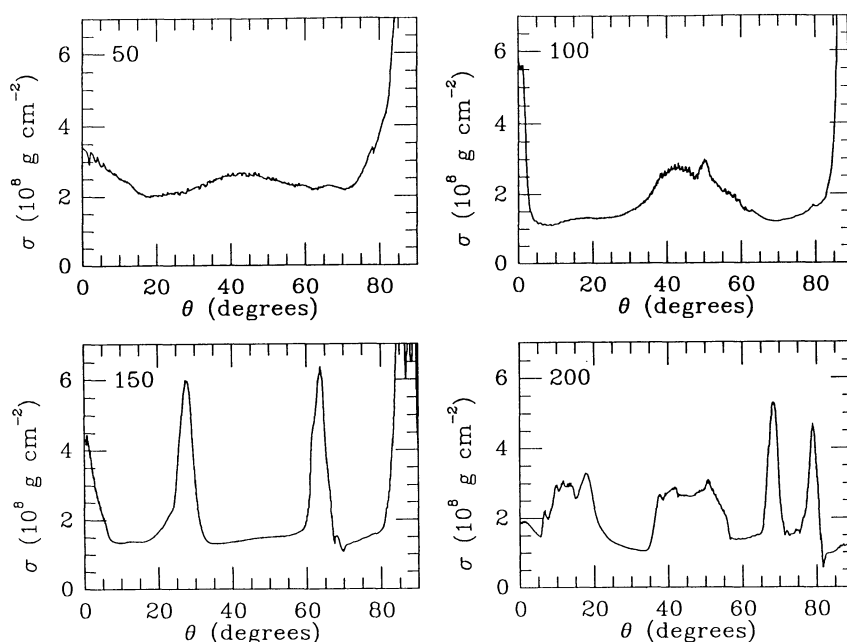


FIG. 16.—Attenuation σ versus angle for resolutions of 50^2 , 100^2 , 150^2 , and 200^2 , an elapsed time of $1.3 \times 10^4 \text{ s}$, and a seed amplitude of 10%

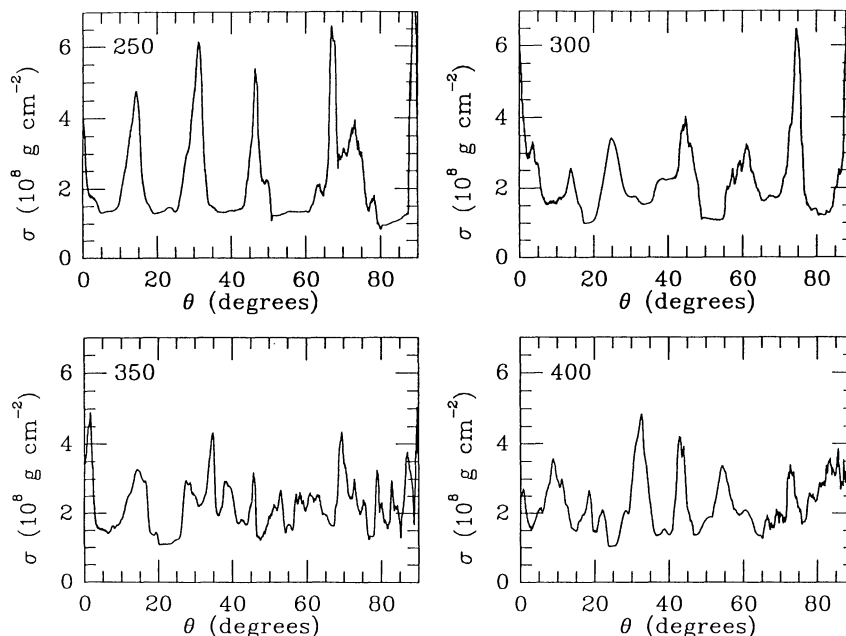


FIG. 17.—Attenuation σ versus angle for resolutions of 250^2 , 300^2 , 350^2 , and 400^2 , an elapsed time of 1.3×10^4 s, and a seed amplitude of 10%

some material is moving at near 2000 km s^{-1} in the 10% case. For an explosion energy of 2×10^{51} ergs, this would scale up to about 2800 km s^{-1} . Note that matter which has left the grid would add components to the H and ^4He curves and would thereby affect line shapes.

We have focused upon the asymmetric development of a spherical shock; in this case, the heavier nuclei (for example, ^{56}Ni) will have a distribution similar to that of ^{24}Mg . Because ^{56}Ni is formed by explosive $^{16}\text{O} + ^{16}\text{O}$ burning in the ^{16}O shell, and such burning will be unlikely to have spherical symmetry (see above), the calculation of the formation of the ^{56}Ni requires at least two dimensions with fine zoning, and, consequently, significantly more computer resources than our one-dimensional calculation of the early stages (see § III above). It may be affected by the nature of the explosion mechanism. In view of these complications, we chose to examine the simpler case first.

IX. DECAY OF ^{56}Ni AND ^{56}Co

a) Simplest Case

What effect will the decay of ^{56}Ni and ^{56}Co have? Consider the evolution of an opaque ^{56}Ni sphere. The decay of ^{56}Ni (mean life of 8.8 days) releases about 2 Mev, which corresponds to an energy $Q \simeq 4 \times 10^{16}$ ergs s^{-1} . If this is converted into heat, and then by expansion into bulk motion of the ^{56}Ni and daughter ^{56}Co , the mean velocity is $v_{\text{rms}} \simeq \sqrt{2Q} = 2.8 \times 10^3 \text{ km s}^{-1}$ (note that the velocity at the edge of the sphere is larger by a factor of $\sqrt{5/3} = 1.291$ as in Arnett 1982, or $v_{\text{edge}} \simeq 3.6 \times 10^3 \text{ km s}^{-1}$). If there is an initial homologous expansion of the sphere, with an edge velocity of 10^3 km s^{-1} as suggested by the one-dimensional hydrodynamic calculations (e.g., Arnett 1988a, b), these numbers become $v_{\text{rms}} \simeq 2.9 \times 10^3 \text{ km s}^{-1}$ and $v_{\text{edge}} \simeq 3.8 \times 10^3 \text{ km s}^{-1}$.

How does this compare with observations? Witteborn *et al.* (1989) found a mean velocity of $v_{\text{rms}} \sim 2.0 \times 10^3 \text{ km s}^{-1}$ for Ni and Co. If the distribution were uniform, the velocity at the edge would be $v_{\text{edge}} \sim 2.6 \times 10^3 \text{ km s}^{-1}$. These velocities are

smaller than the estimates above. Haas *et al.* (1990) have interpreted their observations to indicate edge velocities $v_{\text{edge}} > 3 \times 10^3 \text{ km s}^{-1}$, with a feature at $v \simeq 3.8 \times 10^3 \text{ km s}^{-1}$ containing 3% of the matter which was originally ^{56}Ni . A more accurate determination of the distribution of these larger velocities is highly desirable.

By the time the ^{56}Co decays, the supernova ejecta are so tenuous that radioactive heating is not restricted to the decaying matter itself but is spread over a much larger mass. Therefore, hydrodynamic effects due to differential heating are likely to be more pronounced for ^{56}Ni decay.

b) The Effects of Other Matter

The rough agreement of the estimates just given is somewhat illusory. In the case of a supernova, the ^{56}Ni must snowplow into or punch through other material, slowing down to some extent. Suppose our opaque ^{56}Ni sphere moves into a surrounding shell. First, we note that the sound speed just outside the ^{56}Ni will be less than the expansion velocity, because of expansion since the explosion shock passed. The edge velocity is larger than this initial expansion velocity by a factor of almost 4, so that the expansion of the ^{56}Ni (^{56}Co) into the overlying matter must be supersonic, generating a shockwave (see Arnett 1988a, b).

Suppose the ^{56}Ni (^{56}Co) uniformly penetrates the overlying matter, without slowing—a simplistic but interesting case. Then it will catch all matter expanding at a velocity less than $v_{\text{edge}} \simeq 3.8 \times 10^3 \text{ km s}^{-1}$. For an initial velocity at the edge of the ^{56}Ni of $v_0 \sim 10^3 \text{ km s}^{-1}$, and assuming essentially homologous expansion, we have for the mass M which is swept up

$$M = M_{\text{Ni}}(v/v_0)^3 \sim 3.8 M_{\odot},$$

for $M_{\text{Ni}} = 0.07 M_{\odot}$. Thus, essentially all the matter interior to the ^4He shell will be penetrated. In reality, we might expect some ^{56}Ni to be slowed and some to be accelerated more. Again, we need to extract the *distribution* of velocities from the observations.

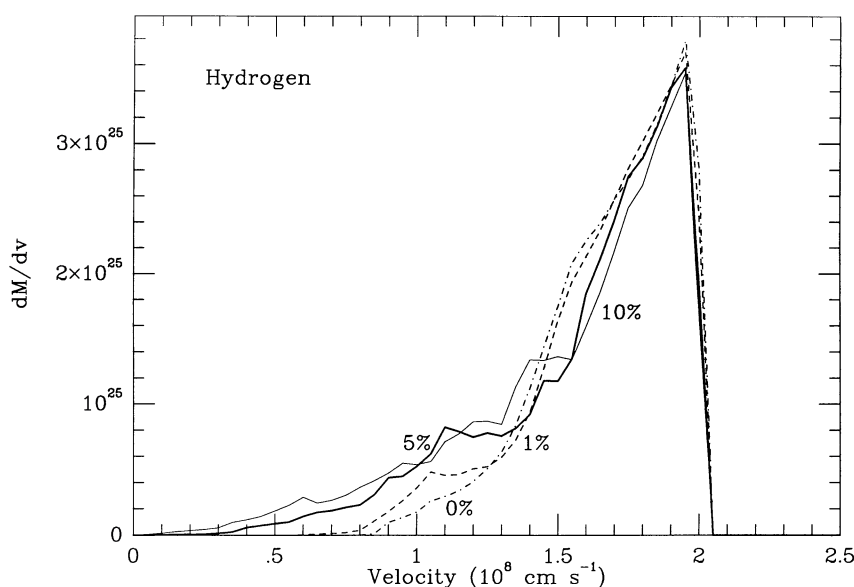


FIG. 18a

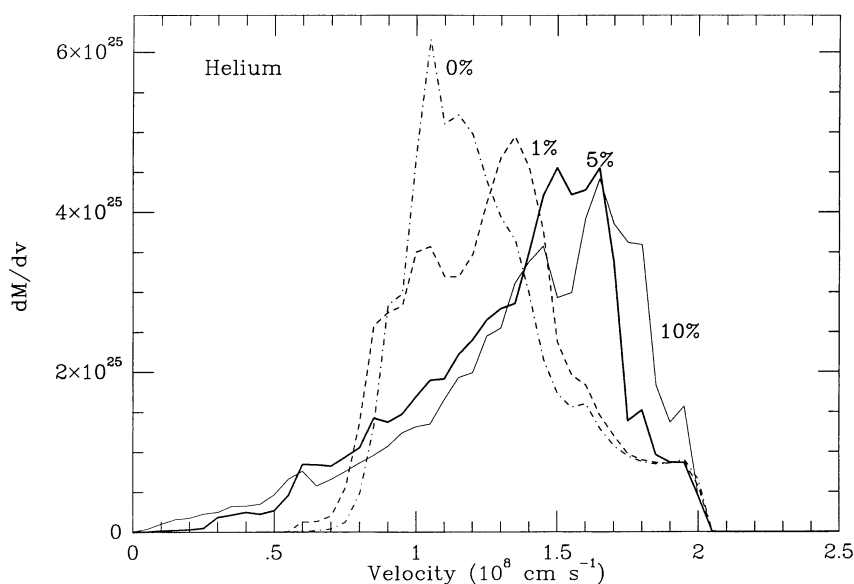


FIG. 18b

FIG. 18.—Abundances of four representative nuclei, (a) H, (b) ^4He , (c) ^{16}O , and (d) ^{24}Mg , in terms of the mass per unit velocity interval dM/dv versus radial velocity v . The different curves correspond to initial random seed of amplitudes of 0% (grid noise), 1%, 5%, and 10%. The H curve is truncated because faster moving H has left the computational grid and is not plotted. Asymmetric motion causes “diffusion” in velocity space, given matter with both higher and lower velocities than for spherically symmetric motion. The velocity scale would be larger by a factor of 1.4 if the explosion energy were 2×10^{51} ergs, a value also acceptable from fits of this initial model to the light curves and doppler shifts (Arnett 1988a, b).

If the ^{56}Ni is already mixed, as the hydrodynamic calculations suggest, then we may repeat this analysis with a larger edge velocity prior to ^{56}Ni decay: $v_0 \sim 2 \times 10^3 \text{ km s}^{-1}$. By conservation of energy (again, no sharing with matter passed by),

$$v_{\text{edge}}^2 = \sqrt{v_0^2 + \frac{10}{3} Q} \sim 4.1 \times 10^3 \text{ km s}^{-1},$$

so that, for the mass M which is swept up,

$$M = M_{\text{Ni}}(v/10^3 \text{ km s}^{-1})^3 \sim 5 M_{\odot},$$

for $M_{\text{Ni}} = 0.07 M_{\odot}$. This implies penetration of the hydrogen envelope.

It should be clear from preceding sections that such estimates, while suggestive, are quite simplistic. Note that the velocities we have calculated for the ^{24}Mg , which typify the heavy elements, are already a significant fraction of the observationally inferred values. This is especially true if we use an equally plausible explosion energy of 2×10^{51} ergs, so that the velocities are larger by a factor of 1.4. Even with the smaller energy, the acceleration expected from ^{56}Ni heating may be just what is needed for agreement. It will be interesting to see if numerical calculations predict any observable difference between these possibilities. In any case, the observed scale of mean velocity seems quite consistent with expectations. A more detailed discussion is being prepared for publication.

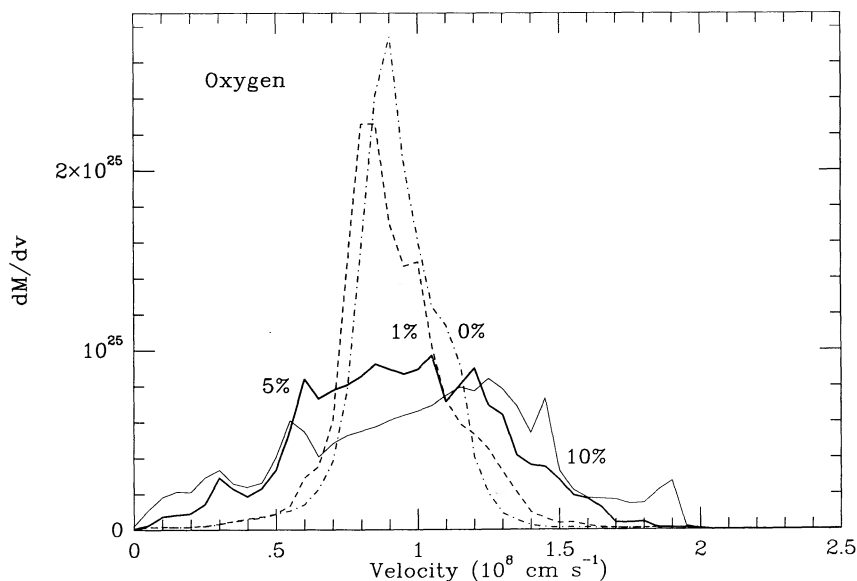


FIG. 18c

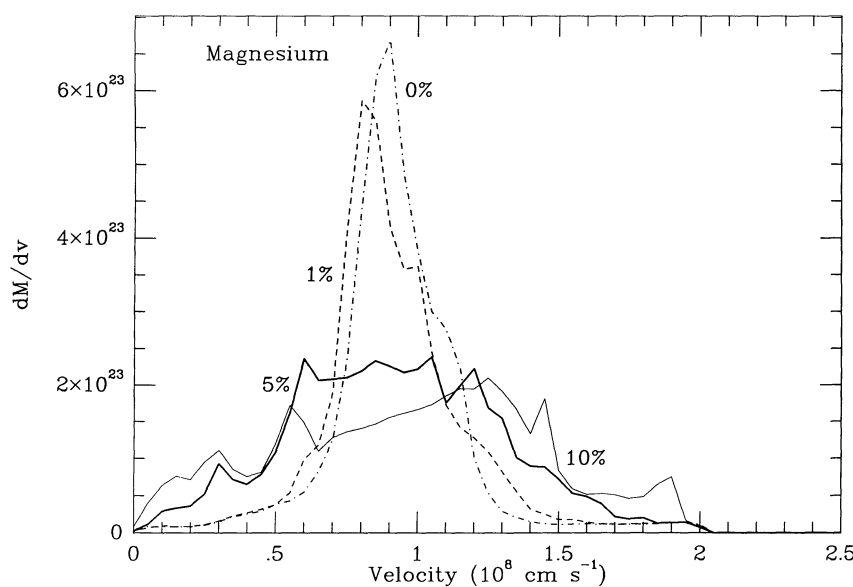


FIG. 18d

X. CONCLUSIONS

a) *Fracturing of Mantle*

These calculations suggest that by the time the shock has reached the surface of the presupernova, the spherical symmetry of the mantle was severely fractured. No special asymmetry in the explosion is required, nor is it indicated. This confirms the previous result of AFM, which was the first reasonably well-resolved multidimensional hydrodynamic calculation of instabilities in a Type II supernova. At this time, about several hours after core collapse, ^{56}Ni and ^{56}Co decay have not had time to be effective in heating the matter. There is no ^{56}Ni "bubble," but rather, ^{56}Ni shrapnel. The existence of this fracturing is not sensitive to the choice of initial model of the star (see Hachisu *et al.* 1990), provided a reasonably accurate presupernova model is used. Similarly, it is insensitive to the choice of seed perturbations, provided they lie in the range

expected from the evolutionary calculations of the presupernova. While more exotic situations are not ruled out if their effects are small, they do not seem to be required.

The clumping and mixing seem to be appropriate to explain a wide variety of phenomena observed and attributed to asymmetry, mixing, or clumping. The velocities are lower than observed in SN 1987A for an explosion of 1×10^{51} ergs but become interesting for 2×10^{51} ergs.

b) *SN Ib Mass Estimates*

The degree of clumping of matter is so pervasive in these calculations that it seems likely to affect estimates of the mass from modeling the light curve. That is probably not a problem for SN 1987A (most of the mass was in the hydrogen envelope, which may not yet have been highly clumped), but may have new implications from mass estimates for supernovae of Type Ib (see Ensman and Woosley 1988).

c) Resolution of Hydrodynamic Methods

There is a large difference in inherent resolution of Eulerian methods of numerical hydrodynamics, and this difference is important for the problem discussed here. The cruder methods require exceptionally fine zoning to duplicate these results and consequently, massive computer resources. The documentation here of results for a systematic sequence of different resolutions makes it possible to compare the accuracy of different methods.

d) ^{56}Ni and ^{56}Co Decay and Dynamics

If the ^{56}Ni is already mixed, as the hydrodynamic calculations suggest, then the heating is shared with the mixed matter. The resulting acceleration will depend on how this occurs. The velocities of the ^{24}Mg , which typify the heavy elements, are already a significant fraction of the observed mean velocity. Either the acceleration likely from the ^{56}Ni heating or a higher explosion energy (or both) may be just what is needed for agreement; the observed scale of mean velocity seems quite consistent with expectations. A more detailed discussion is being prepared for publication.

REFERENCES

- Arnett, W. D. 1977, *Ap. J.*, **218**, 815.
 ———. 1982, *Ap. J.*, **253**, 785.
 ———. 1986, *IAU Symposium No. 125, The Origin and Evolution of Neutron Stars*, ed. D. J. Helfand and J.-H. Huang, (Dordrecht: Reidel), p. 27.
 ———. 1987, *Proc. ESO Workshop of the SN 1987A*, ed. J. Danziger (Munich: ESO), p. 373.
 ———. 1988a, in *Supernova 1987A in the Large Magellanic Cloud*, ed. M. Kafatos and A. Michalitsianos (Cambridge: Cambridge University Press), p. 301.
 ———. 1988b, *Ap. J.*, **331**, 377.
 Arnett, W. D., Bahcall, J. N., Kirshner, R. P., and Woosley, S. E. 1989, *Ann. Rev. Astr. A.*, **27**, 629.
 Arnett, W. D., Fryxell, B. A., and Müller, E. 1989, *Ap. J. (Letters)*, **341**, L63.
 ———. 1990, in *Proc. Santa Cruz Conf. on Supernovae*, in press.
 Arnett, W. D., and Fu, A. 1989, *Ap. J.*, **340**, 396.
 Arnold, C. N. 1985, Ph.D. thesis, University of Michigan.
 Bandiera, R. 1984, *Astr. Ap.*, **139**, 368.
 Barrett, P. 1987, *Proc. ESO Workshop of the SN 1987A*, ed. J. Danziger (ESO: Munich), p. 173.
 Beam, R. M., and Warming, R. F. 1978, *AIAAJ.*, **16**, 393.
 Benz, W., and Thielemann, F.-K. 1990, *Ap. J. (Letters)*, **348**, L17.
 Bionta, R. M., et al. 1987, *Phys. Rev. Letters*, **58**, 1494.
 Blanco, V. M., et al. 1987, *Ap. J.*, **320**, 589.
 Boris, J. P., and Book, D. L. 1973, *J. Comput. Phys.*, **11**, 38.
 Bussard, R. W., Burrows, A., and The, L. S. 1989, *Ap. J.*, **341**, 401.
 Chevalier, R. A. 1976, *Ap. J.*, **207**, 872.
 ———. 1990, preprint.
 Chevalier, R. A., and Soker, N. 1989, *Ap. J.*, **341**, 867.
 Colella, P., and Glaz, H. M. 1985, *J. Comput. Phys.*, **59**, 264.
 Colella, P., and Woodward, P. R. 1984, *J. Comput. Phys.*, **54**, 174.
 Cook, W. R., Palmer, D., Prince, T., Schindler, S., Starr, C., and Stone, F. 1988, *IAU Circ.*, No. 4527.
 Couch, W. J. 1988, in *Supernova 1987A in the Large Magellanic Cloud*, ed. M. Kafatos and A. Michalitsianos (Cambridge: Cambridge University Press), p. 61.
 Dotani, T., et al. 1987, *Nature*, **330**, 230.
 Ebisuzaki, T., and Shibasaki, N. 1988, in *Supernova 1987A in the Large Magellanic Cloud*, ed. M. Kafatos and A. Michalitsianos (Cambridge: Cambridge University Press), p. 398.
 Ensmann, L. M., and Woosley, S. E. 1988, *Ap. J.*, **333**, 754.
 Erickson, E. F., Haas, M. R., Colgan, S. W. J., Lord, S. D., Burton, M. G., Wolf, J., Hollebach, D. J., Werner, M. 1988, *Ap. J. (Letters)*, **330**, L39.
 Falk, S. W., and Arnett, W. D. 1973, *Ap. J. (Letters)*, **180**, L65.
 Fransson, C., and Chevalier, R. A. 1989, *Ap. J.*, **343**, 323.
 Fryxell, B. A., Müller, E., and Arnett, W. D. 1989, in *Numerical Methods in Astrophysics*, ed. P. Woodward (Harcourt Brace), in press.
 Fu, A., and Arnett, W. D. 1989, *Ap. J.*, **340**, 414.
 Godunov, S. K. 1959, *Nat. Sb.*, **47**, 271.
 Grebenev, S. A., and Syunyaev, R. A. 1988, *Sov. Astr. Letters*, **14**, 675.
 Haas, M. R., Colgan, S. W. J., Erickson, E. F., Lord, S. D., Burton, M. G., and Hollenbach, D. J. 1989, preprint.
 Hachisu, I., Matsuda, T., Nomoto, K., and Shigeyama, T. 1990, *Ap. J. (Letters)*, **358**, L57.
 Hanuschik, R. W., and Dachs, J. 1987, *Astr. Ap. (Letters)*, **182**, L29.
 Hanuschik, R. W., Thimm, G., and Dachs, J. 1988, *M.N.R.A.S.*, **234**, 41.
 Hawley, J. F., Smarr, L. L., and Wilson, J. R. 1984, *Ap. J.*, **277**, 296.
 Hirata, K. S., et al. 1987, *Phys. Rev. Letters*, **58**, 1490.
 Höflich, P. 1988a, in *Atmospheric Diagnostics of Stellar Evolution: Chemical Peculiarity, Mass Loss, and Explosion*, ed. K. Nomoto (Berlin: Springer), p. 288.
 Höflich, P. 1988b, *Proc. Astr. Soc. Australia*, **7**, 434.
 Karovska, M., Koechlin, L., Nissen, P., Papiailiolos, C., and Standley, C. 1988, *IAU Circ.*, No. 4604.
 Kirshner, R. P. 1988, in *Supernova 1987A in the Large Magellanic Cloud*, ed. M. Kafatos and A. Michalitsianos (Cambridge: Cambridge University Press), p. 87.
 Kumagai, S., Itoh, M., Shigeyama, T., Nomoto, K., and Nishimura, J. 1989, in *Supernova 1987A in the Large Magellanic Cloud*, ed. M. Kafatos and A. Michalitsianos (Cambridge: Cambridge University Press), p. 323.
 Larson, H. P., Drapatz, S., Mumma, M. J., and Weaver, H. A. 1987, in *Proc. ESO Workshop of the SN 1987A*, ed. J. Danziger (Munich: ESO), p. 147.
 Lax, P. D., and Wendroff, B. 1960, *Comm. Pure Appl. Math.*, **13**, 217.
 ———. 1964, *Comm. Pure Appl. Math.*, **17**, 381.
 Lucy, L. B. 1988, in *Supernova 1987A in the Large Magellanic Cloud*, ed. M. Kafatos and A. Michalitsianos (Cambridge: Cambridge University Press), p. 323.
 Matz, S. M., Share, G. H., Leising, M. D., Chupp, E. L., Vestrand, W. T., Purcell, W. R., Strickman, M. S., and Reppin, C. 1988, *Nature*, **331**, 416.
 Monaghan, J. J. 1985, *Computer Phys. Reports*, **3**, 71.
 Monaghan, J. J., and Varnas, S. R. 1988, *M.N.R.A.S.*, **231**, 515.
 Müller, E., Fryxell, B. A., and Arnett, W. D. 1990a, in *The Chemical and Dynamical Evolution of Galaxies*, ed. F. Ferrini, F. Matteucci, and J. Franco, (Pisa: Casa Editrice Giardini).
 ———. 1990b, preprint.
 Müller, E., Hillebrandt, W., Orio, M., Höflich, P., Mönchmeyer, R., and Fryxell, B. 1989, *Astr. Ap.*, **220**, 167.
 Nagasawa, M. 1990, preprint.
 Nagasawa, M., Nakamura, T., and Miyama, S. 1989, *Pub. Astr. Soc. Japan*, **40**, 691.
 Nomoto, K., Shigeyama, T., and Hashimoto, M. 1987, in *Proc. ESO Workshop of the SN 1987A*, ed. J. Danziger (Munich: ESO), p. 235.
 Phillips, M. 1988, in *Supernova 1987A in the Large Magellanic Cloud*, ed. M. Kafatos and A. Michalitsianos (Cambridge: Cambridge University Press), p. 17.
 Phillips, M. M., and Heathcote, S. R. 1989, *Pub. A.S.P.*, **101**, 137.
 Rank, D. M., et al. 1988, *Nature*, **331**, 505.
 Rester, A. C., Eichorn, G., and Coldwell, R. L. 1988, *IAU Circ.*, No. 4526.
 Sandie, W., Nakano, G., and Chase, L. 1988, *IAU Circ.*, No. 4526.
 Schwarz, H. E. 1987, in *Proc. ESO Workshop of the SN 1987A*, ed. J. Danziger (Munich: ESO), p. 167.
 Shigeyama, T., and Nomoto, K. 1990, preprint.
 Shull, M., and Xu, Y. 1988, in *Supernova 1987A in the Large Magellanic Cloud*, ed. M. Kafatos and A. Michalitsianos (Cambridge: Cambridge University Press), p. 373.
 Spyromilio, J., Meikle, W. P. S., and Allen, D. A. 1990, preprint.
 Stathakis, R., and Cannon, R. D. 1988, *AAO Newsletter*, 45.
 Sunyaev, R. A., et al. 1987, *Nature*, **330**, 227.
 van Leer, B. 1982, *Lecture Notes in Physics*, **170**, 507.
 Wilson, R. B., et al. 1988, in *Nuclear Spectroscopy of Astrophysical Sources*, ed. N. Gehrels and G. Share (New York: AIP), p. 66.
 Witteborn, F., Rank, D. M., Bregman, J. D., Pinto, P. A., Wooden, D., and Axelrod, T. S. 1989, *Ap. J. (Letters)*, **338**, L9.
 Woodward, P. R., and Colella, P. 1984, *J. Comput. Phys.*, **54**, 115.
 Woosley, S. E. 1988, in *Supernova 1987A in the Large Magellanic Cloud*, ed. M. Kafatos and A. Michalitsianos (Cambridge: Cambridge University Press), p. 289.
 Yamada, S., and Sato, K. 1990, preprint.

DAVID ARNETT and BRUCE FRYXELL: Department of Physics, University of Arizona, Tucson, AZ 85721

EWALD MÜLLER: Max-Planck-Institut für Astrophysik, 1 Schwarzschild Strasse, Garching bei München, Germany